High Temperature Mechanical Properties of Rapidly Quenched Zr$_{50}$Ni$_{27}$Nb$_{18}$Co$_5$ Amorphous Alloy

S. Jayalakshmi and E. Fleury[*]

Center for Advanced Functional Metals, Korea Institute of Science & Technology (KIST),
Hawalgok-dong, Seongbuk-gu, Seoul 136-791, Korea

The high temperature mechanical properties of Zr$_{50}$Ni$_{27}$Nb$_{18}$Co$_5$ amorphous ribbons, proposed as metallic membrane material for hydrogen purification are presented. The mechanical behavior of the amorphous alloy, which generally does not exhibit a super-cooled liquid region, can be categorized into varying temperature regimes. A strain rate dependent phenomenon was observed between 425 °C < T < 490 °C in the strain rate range of 10^{-6}s^{-1} to 10^{-2}s^{-1}. However, the alloy did not exhibit Newtonian-flow characteristics at the varied test temperature and strain rate range employed in this study. Detailed analyses indicated that in these temperature regimes structural changes occur, resulting in the formation of nanocrystalline phases. The results from these mechanical tests corroborated with the microstructural changes that occurred at these temperatures/strain rates.

Keywords: amorphous alloys, high temperature properties, tensile, structure, nanocrystals

1. INTRODUCTION

Recently, investigations on the mechanical properties of metallic glasses have been gaining importance due to their viscous nature, especially with superplasticity in a certain temperature regime below the crystallization temperature. Several alloy compositions as described in [1-5] exhibited a Newtonian viscous behavior in the super-cooled liquid region that has been defined as the temperature range between the glass transition (T$_g$) and crystallization (T$_x$). Such a behavior is very inviting for new applications, like micro-molding or micro-forming of components for MEMS/NEMS devices [6-8]. However, together with other possible applications, metallic alloys with an amorphous structure have recently been proposed as candidate materials for permeation membranes for the purification of hydrogen [9-14]. Although these membranes generally operate in a range of temperature lower than the glass transition temperature, T$_g$, their chemical and mechanical stability are important. Hence, investigating the mechanical properties of those hydrogen permeable alloys at higher temperatures is very critical.

Starting with the Ni$_{60}$Nb$_{40}$ amorphous alloy (defined as a metallic glass without any detectable T$_g$ from DSC analyses), Inoue and co-workers investigated the effect of several alloy-ing elements on the hydrogen permeability, and eventually proposed the Zr$_{50}$(Ni$_{0.6}$Nb$_{0.4}$)$_{45}$Co$_5$ as the most optimal composition [9,10]. Amorphous ribbons of this composition demonstrated excellent hydrogen permeability, as high as those of Pd-Ag and Pd-Cu alloys in the temperature range of 300 °C to 400 °C [10]. In contrast to studies that aimed at increasing the glass forming ability of metallic glass, the composition of this alloy has been tailored for properties required for candidate materials to be used for hydrogen permeable membranes, i.e., high hydrogen solubility, high hydrogen diffusivity, and a low permeation for other gases (high hydrogen selectivity). Furthermore, it was recently demonstrated that the Zr-Ni-Nb-Co amorphous alloy exhibited good room temperature embrittlement resistance as well, with strength retention characteristics upto 20 at.% of hydrogen [15]. However, it was observed that during long term gaseous hydrogen permeation experiments at high temperatures, the ribbons lost their mechanical stability and fractured into powders when the temperature was brought back to room temperature at the end of the permeation test [16,17]. This stimulated the current study on the high temperature mechanical properties of this alloy, and the effect of temperature and strain rate on the tensile properties of Zr$_{50}$Ni$_{27}$Nb$_{18}$Co$_5$ amorphous ribbons are presented in this paper. The structural and thermal properties of the mechanically tested alloy were analyzed with the aim of understanding its high temperature behavior.

*Corresponding author: efleury@kist.re.kr

2. EXPERIMENTAL PROCEDURE

$Zr_{50}Ni_{27}Nb_{18}Co_5$ amorphous alloy ribbons of 15 mm width and 40 μm thickness were manufactured by Amosense Ltd., Korea, by using a single roller melt spinning technique. The initial thermal properties of the alloy were studied using a Differential Scanning Calorimetry (DSC) at varying heating rates (5 K/min to 80 K/min). The structure of the alloy at room and high temperatures were analyzed using X-ray diffraction (XRD, Cu-K_α). The mechanical tests were performed in a 2.5 ton universal tensile testing machine in air at varying temperatures and strain rates. The alloy specimens that were bone shaped, with 25 mm gauge length and 5 mm width, were used as test samples. The tensile tests were conducted at high temperatures using a furnace with a temperature control of up to ± 3 °C, with the samples being mounted on Ni-based high temperature tensile grips. The strain rates used in the present study varied between 10^{-6} to $10^{-2} s^{-1}$. The experiments were performed at temperatures that ranged from room temperature to 550 °C. The specimens were always loaded into the furnace after the desired test temperature was reached, and was held at that temperature for 30 min. After each tensile experiment, the furnace was immediately opened and the specimen was cooled to room temperature. Tests were conducted in order to acquire at least the 3 closest repeatable values in each test condition, and the plotted values were obtained from their average. Bend tests were also conducted in the high temperature furnace in order to observe the change in ductility of the alloy at these temperatures. The test method involved placing a U-shaped specimen between two parallel flat platens and measuring the radius of curvature during bending until fracture occurs [18,19]. The samples were held at the test temperature for 90 min before the experiment started. The bending experiments were performed at a controlled platen velocity of 1.66×10^{-6} ms^{-1}. The strain to fracture, ε_f in %, was calculated using the equation, $\varepsilon_f = t / (2r - t) \times 100$, where t is the thickness of the specimen and r is the radius of curvature at fracture [19-21].

After the mechanical tests, the structure and thermal properties of the ribbons were analyzed by using XRD and DSC, and the fracture surfaces were studied using Scanning Electron Microscopy (SEM). The thickness of the oxide layers formed, if any, was measured using Auger Electron Spectroscopy (AES). Further, detailed structural analyses of the mechanically tested samples were performed using High Resolution Transmission Electron Microscopy (HRTEM) in order to observe the ribbon microstructure and its possible modifications that were induced by mechanical testing.

3. RESULTS

Figure 1(a) shows the initial thermal properties of the $Zr_{50}Ni_{27}Nb_{18}Co_5$ ribbon obtained from the DSC traces for different heating rates. The alloy exhibits two crystallization transition peaks, the onsets of which are at the heating rate of 80 K/min, 490 °C, and 603 °C, respectively. As the DSC traces indicate the kinetics of crystallization of an alloy, the lower the heating rate, the longer is the time available for atomic motion, and thus the lower the temperature of phase transformation. This is evident from the shift of crystallization temperatures towards lower values with decreasing heating rates. Further, this alloy, which has been developed for hydrogen permeation application, does not have a specific glass transition temperature, T_g, and hence does not possess a super-cooled liquid region. The crystallization temperature (T_x) and the enthalpy of crystallization (ΔH) of both the peaks decrease with a decreasing heating rate. Plotted in the inset are the extrapolated onset temperatures that are $T_{x1}^o = 458$ °C and $T_{x2}^o = 546$ °C, respectively, which are comparable to those reported by Yamaura *et al.* [10]. Figure 1(b) shows the activation energy for crystallization determined by Kissinger's analysis. The activation energies for the crystallization products are 425 kJ/mol and 343 kJ/mol, respectively, indicating that the second exothermic transition has a lower energy barrier for crystallization than the first crystallization peak.

Figure 1(c) shows the Time-Temperature-Transformation (T-T-T) diagram of the alloy that was obtained by isothermal annealing of specimens in the DSC, performed between 460 °C and 580 °C. The T-T-T diagram is a plot of temperature versus log time and gives an indication of the beginning and end of transformation obtained at a constant temperature (isothermal) without applied stress. In an amorphous alloy, where the alloy is heated at a constant temperature well below the crystallization temperature, crystallization does occur after a prolonged time period. The rate of this transformation invariably depends on the activation energy of the crystalline phase. The time for such transformation was recorded for several isothermal-heating temperatures, and provides a description of the time dependency of amorphous-to-crystal transformation behavior.

It should be noted here that from the work of Inoue and co-workers [10], although the extrapolated values of T_{x1}^o was 458 °C, the maximum operating temperature of the alloy for permeation was limited to 400 °C, which may be due to the possible formation of crystalline phases above that temperature during the long term test in a hydrogen environment. From Fig. 1(d) that shows the XRD traces that were conducted in an argon atmosphere at different temperatures, the as-spun specimen is found to be completely amorphous at room temperature, while the formation of crystalline phases (Zr_2Ni nanocrsytals) occurs only at temperatures beyond 440 °C. At temperatures higher than the crystallization temperature, dominant Zr_2Ni and $ZrNi$ phases, together with $Ni_{11}(Zr,Nb)_9$ phase, are also formed. In Fig. 1(d), the alumina
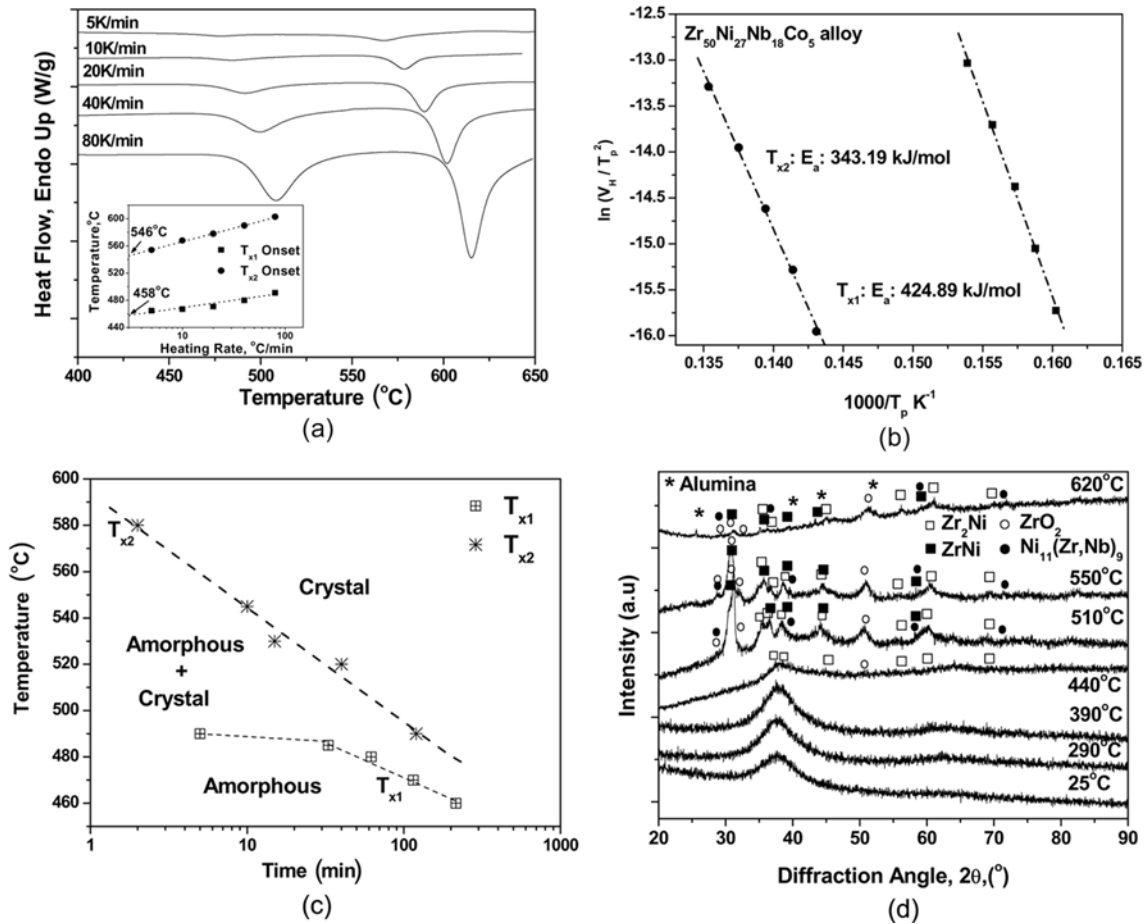
Fig. 1. (a) DSC traces of Zr$_{50}$Ni$_{27}$Nb$_{18}$Co$_5$ alloy at various heating rates. Inset shows the onset temperatures of crystallization at these heating rates, (b) Kissinger's plot showing the activation energy for crystallization for the Zr$_{50}$Ni$_{27}$Nb$_{18}$Co$_5$ alloy, (c) Time-Temperature-Transformation diagram for the Zr$_{50}$Ni$_{27}$Nb$_{18}$Co$_5$ alloy generated from isothermal DSC data, showing the amorphous, composite and crystalline regions, (d) XRD patterns at room and high temperature for the Zr$_{50}$Ni$_{27}$Nb$_{18}$Co$_5$ alloy.

peaks arise from that of the high temperature sample holder.

Figure 2 shows the variation of the fracture strain with temperature obtained from bend ductility tests, conducted at varying temperatures. It can be observed from the figure that the alloy is ductile until ~445 $^{\circ}$C, wherein it can be bent to 180° without fracture till that temperature. However, with a further increase in test temperature, there is a drastic transition from ductile-to-brittle behavior, as the temperature is in the proximity of the first crystallization temperature. This result suggests that the permeation can be performed until ~440 $^{\circ}$C, without any loss of mechanical ductility.

Figure 3(a) shows a representative stress-strain behavior of the alloy that was tested at a strain rate of 10^{-3} s^{-1} between room temperature to 550 $^{\circ}$C. From this figure the following observations can be made: (i) at low temperatures (T < 390 $^{\circ}$C), the alloy exhibits inhomogeneous deformation behavior, which is typical of amorphous alloys, characterized by vein patterns on the fracture surface (see SEM image, Fig. 3(b)), (ii) for 390 $^{\circ}$C T 440 $^{\circ}$C, the alloy deforms with large elongation and the mechanical behavior is characterized by a
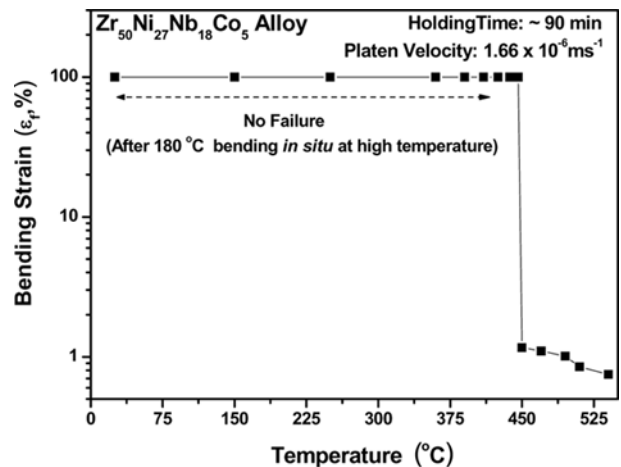

Fig. 2. Variation of bending fracture strain with temperature obtained from bend test.

distinct stress-overshoot, the magnitude of which decreases when the test temperature and strain rate increase, (iii) for 440 $^{\circ}$C < T 490 $^{\circ}$C, homogenous flow occurs without stress
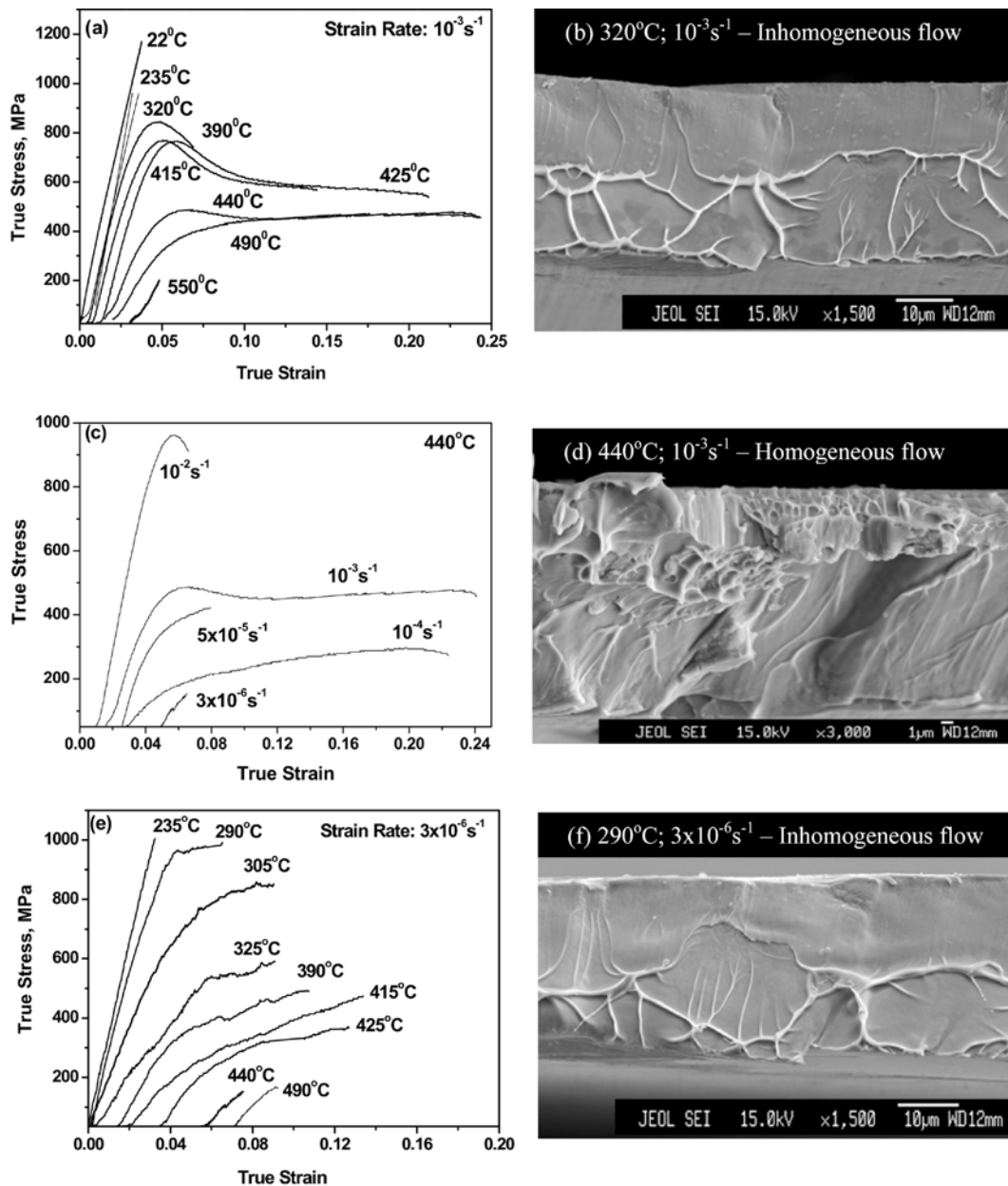
Fig. 3. Tensile stress-strain behavior of the alloy (a) & (e) from room temperature to 550 °C at $\dot{\varepsilon} = 10^{-3}$ s^{-1} and $\dot{\varepsilon} = 10^{-6}$ s^{-1} respectively and (c) at 440 °C from $\dot{\varepsilon} = 10^{-6}$ s^{-1} to $\dot{\varepsilon} = 10^{-2}$ s^{-1}. (b), (d) and (f) are the SEM images that show the tensile fracture morphologies of the alloy at various testing parameters.

overshoot and the maximum elongation is obtained in this regime, (iv) for 490 °C < T 550 °C, the alloy shows no significant plasticity and fails in a brittle manner.

Figure 3(c) shows the representative behavior of the alloy at different strain rates at a constant temperature, here 440 °C, i.e., just below the ductile-to-brittle transition temperature. At this temperature, and as the strain rate decreased from 10^{-2} to 10^{-4} s^{-1}, the behavior of the alloy varies from brittle with inhomogeneous deformation to ductile with homogenous flow (see SEM image 3(d)). Also, the behavior obtained for

a strain rate of 10^{-3} s^{-1}, and characterized by a ductile behavior with prominent stress overshoot, appears to be a transitional state. The stress overshoot has been attributed to the change in the visco-elastic properties of the alloy as a result of structural relaxation and an increased atomic mobility at the yield stress due to a gradual increase in the free volume that decreases the viscosity [22,23]. For the Zr-Ni-Nb-Co amorphous ribbon, the magnitude of the stress-overshoot in that transition regime was found to decrease with decreasing strain rate until it reached the homogeneous flow, which is in

accordance with Kawamura *et al.* and Kim's results [22, 24,25]. However, the elongation to fracture is limited to a few percent and the alloy specimen fails in a brittle manner when tested under strain rates below 10^{-4} s^{-1}. The mode of deformation and the elongation at rupture obtained during these tests are thus strongly dependent on the applied strain rate, i.e., time-dependent. Another interesting feature observed is that of Fig. 3(e), which shows the stress-strain behavior at varying temperatures for a strain rate of 3×10^{-6} s^{-1}. It can be seen that at such low strain rates, a plastic deformation is observed under tensile mode at temperatures as low as 290 °C, even though it is also showing inhomogeneous flow behavior (see SEM image, Fig. 3(f)), i.e., at a temperature that is about 160 °C to 170 °C lower than the first crystallization peak temperature. Similarly, Sergueeva and co-workers have reported an enhanced ductility in tension and compression in Vitreloy 1 at a low temperature, even at high strain rates [26].

It is well known that unlike conventional crystalline alloys where plastic deformation is explained by the theory of dislocation, the plastic deformation in amorphous alloys occurs by shear localization at low temperature [27]. Under mechanical loading conditions (such as tensile loading here), and at temperatures well below the glass transition temperature, the stress is insensitive to the strain rate and the flow is characterized by a plastic and inhomogeneous behavior [1]. The non-elastic deformation is confined to narrow bands called 'shear bands' (inhomogeneous flow), and fracture eventually occurs due to excessive localized deformation of such dominant shear bands [1]. However, at higher temperatures, as for example observed in the super-cooled liquid region and at low stress, the tensile specimens deform uniformly (homogenous flow) and extensive plastic deformation occurs [28]. When the variation of stress is directly proportional to the variation of strain rate, the viscous flow is described as Newtonian, whereas for stress varying non-linearly with the strain rate, the stress can be correlated to the strain rate by the equation, $\sigma = k \dot{\varepsilon}_p^m$ with m < 1, which is known as the non-Newtonian flow [28]. Though several studies have reported a Newtonian flow for metallic glasses [1-5], not all alloys undergo a Newtonian-flow behavior in the super-cooled liquid region [29-31].

Figure 4(a) shows the variation of peak stress with strain rate obtained from the stress-strain curves. In the present case, the value of strain-rate sensitivity, m, where $m = \Delta \log \sigma / \Delta \log \dot{\varepsilon}$ [29], is always < 0.3, indicating that a Newtonian flow was not observed in this alloy, which is indeed not surprising since the Zr-Ni-Nb-Co amorphous alloy does not exhibit a super-cooled liquid region. Furthermore, the dependency of the strain rate sensitivity, m, with temperature can be observed in the inset of Fig. 4(b), where the 'm' value is relatively low at T < 400 °C, and the value of 'm' steeply increases between 415 °C to 425 °C, where it reaches a maximum around 0.25, then decreases . As observed in the bend
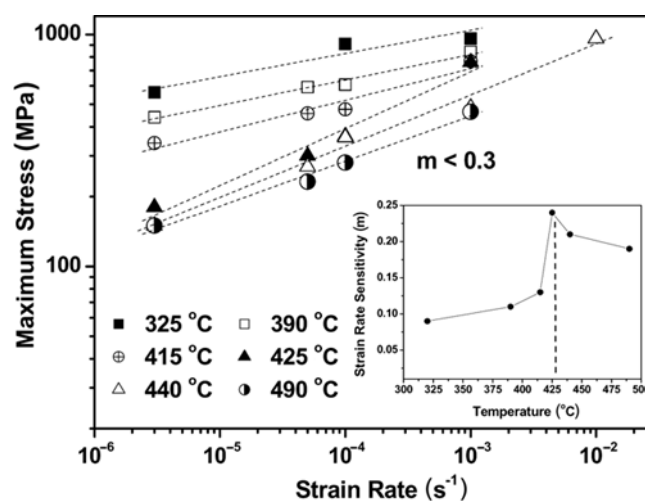

Fig. 4. Tensile stress - strain rate relationship in Zr$_{50}$Ni$_{27}$Nb$_{18}$Co$_{5}$ alloy at various test temperatures. The value of strain rate sensitivity, m, indicate a non-Newtonian flow behavior (b) variation of strain rate sensitivity with temperature.

tests data, this result indicates a transition in the strain rate sensitivity in a similar temperature range (425 °C-440 °C). While superplastic-like flow behavior with Newtonian flow and m ~1 for metallic glasses is quite common under compressive loading, very few studies have reported such a behavior under tension [2,22,24,25,32,33]. For the Zr-Ni-Nb-Co alloy (from extrapolation to zero heating rate, $T_{x1}^o = 458$ °C), while the 'm' value seems to increase beyond 415 °C, the increase of the 'm' value, which would be expected for a Newtonian flow, seems to be hindered by a microstructural instability, resulting in a loss of ductility. Hence, in the present alloy, a non-Newtonian flow behavior was observed at all temperatures within the examined strain rate range. It will be shown below that such non-Newtonian behavior can be attributed to structural instability arising from nanocrystallization during high temperature deformation [2,28,30,35].

Figures 5(a) and (b) show the variation of tensile strength and elongation as a function of the strain rate at various temperatures. As observed in the bend tests, which indicated the possible existence of two temperature regimes (showing ductile and brittle behavior), it is quite evident from these figures that the mechanical behavior under tensile mode can be categorized into four temperature regimes.

According to Fig. 5(a), for T << 390 °C (Regime I), the tensile behavior of the alloy is essentially independent of the strain rate, suggesting that the behavior of the material at this temperature range is not viscous, but plastic [27,34], and characterized by an inhomogeneous flow. For the temperature in Regime II: 390 °C < T < 425 °C, the flow stress is independent of the strain rate for lower strain rates (< 10^{-4} s^{-1}), whereas it increases with an increase in strain rate for $\dot{\varepsilon} > 10^{-4}$ s^{-1}. In the temperature regime of 425 °C ≤ T ≤ 490 °C (Regime
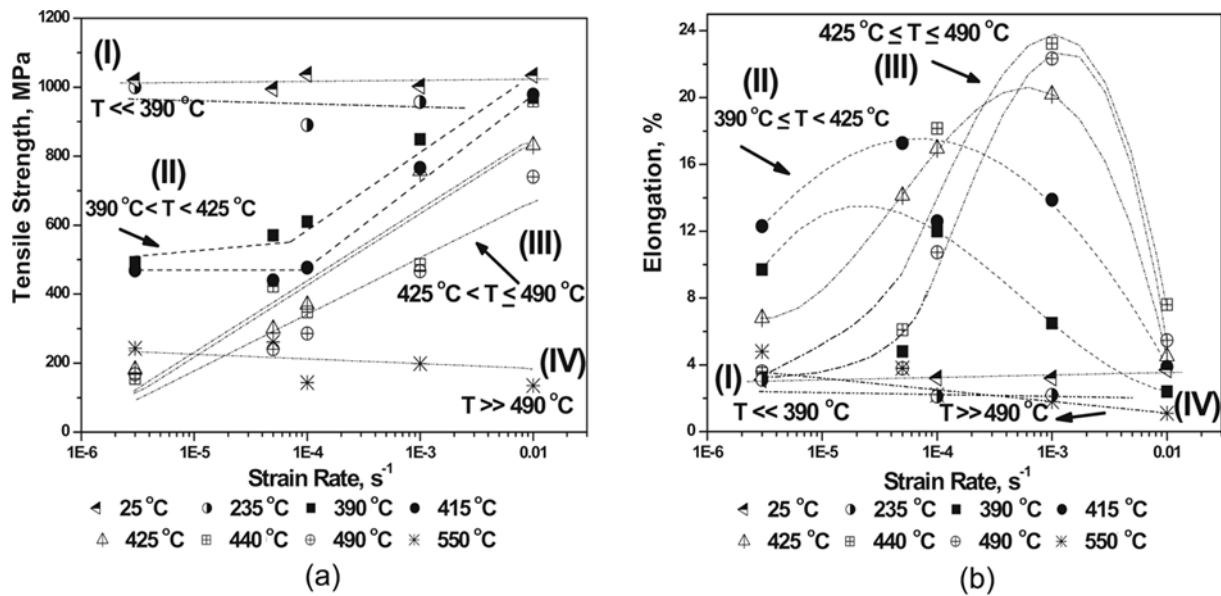
Fig. 5. Strain rate dependency of (a) strength and (b) ductility, in $Zr_{50}Ni_{27}Nb_{18}Co_5$ alloy tested at various temperatures. Note the existence of different temperature regimes that define the behavior.

III), an overall dependency of the flow stress on the strain rate, though non-linear, is observed at all strain rates. (Note that the lines were drawn to guide the eye). However, at high temperatures (Regime IV: $T \gg 490$ °C), the insensitivity of flow stress with the applied strain rate can be attributed to significant structural changes occurring at those temperatures [2,27,29,34], i.e., behavior of a crystalline alloy, and the specimens failed in a brittle manner, with little deformation.

In the entire range of test temperatures and strain rates, a maximum of only ~25 % elongation was obtained for the Zr-Ni-Nb-Co amorphous ribbons, which is much lower than the values obtained by Kawamura *et al.* [22] and Kim *et al.* [32] for $Zr_{65}Cu_{15}Ni_{10}Al_{10}$ glassy alloys in the bulk and ribbon forms in an almost comparable strain rate range. In the temperature regime of 300 °C to 500 °C, which is commonly used for hydrogen permeation in metallic membranes, the variation of elongation with strain rate exhibits two distinct trends (Fig. 5(b)). In the low temperature region II, the elongation decreases with an increase in the strain rate ($> 10^{-5}$ s^{-1}) and temperature. In the high temperature region III (425 °C to 490 °C), the elongation increases with the strain rate with a maximum value obtained at 10^{-3} s^{-1}, while it sharply reduces for the highest strain rates. It is important to notice that under a stain rate of 10^{-3} s^{-1}, the maximum deformation was obtained in the temperature range of 440 °C $\leq T \leq 490$ °C, which corresponds to the limit between the transition regime (i.e., ductile with reduced stress-overshoot) and homogeneous flow. However, the elongation to fracture decreases with a further increase in temperature, possibly due to its proximity to the crystallization temperature. This behavior further illus-

trates the critical role of temperature on the mechanical behavior of the Zr-Ni-Nb-Co amorphous alloy.

4. DISCUSSION

The $Zr_{50}Ni_{27}Nb_{18}Co_5$ amorphous alloy developed by Inoue's group for hydrogen permeation did not exhibit T_g, but could be deformed plastically under tensile mode at temperatures as low as $(T_{x1}^o - 60)$ for a strain rate of 10^{-3} s^{-1} and $(T_{x1}^o - 160)$ under a strain rate of 3×10^{-6} s^{-1}. The mechanical behavior is thus strongly dependent on the applied strain rate, and the strain rate sensitivity varies with the temperature. In order to acquire a better understanding of the dependency of the ductility and the mechanical behavior with the applied strain rate and temperature, the ribbons, both mechanically tested under bending and tensile loading, were analyzed for their thermal and structural properties.

Figure 6(a) shows the DSC traces of the alloy after bend tests at varying temperatures for a holding time of 90 min. From Fig. 6(b), it is evident that with increasing temperature, the enthalpy of formation of the first peak decreases and eventually vanishes when the test temperature reaches ~490 °C, suggesting partial crystallization of the ribbons. However, the enthalpy of the second peak remains almost unaltered until 450 C, and decreases thereupon. With a further increase in test temperature, the crystallization peak disappears and the alloy is no longer amorphous in nature.

Figure 6(c) shows the thermal behavior of the alloy after uniaxial tensile tests at varying strain rates and temperatures. While the DSC patterns obtained after bend tests showed the dependence of the thermal properties of the alloy on the
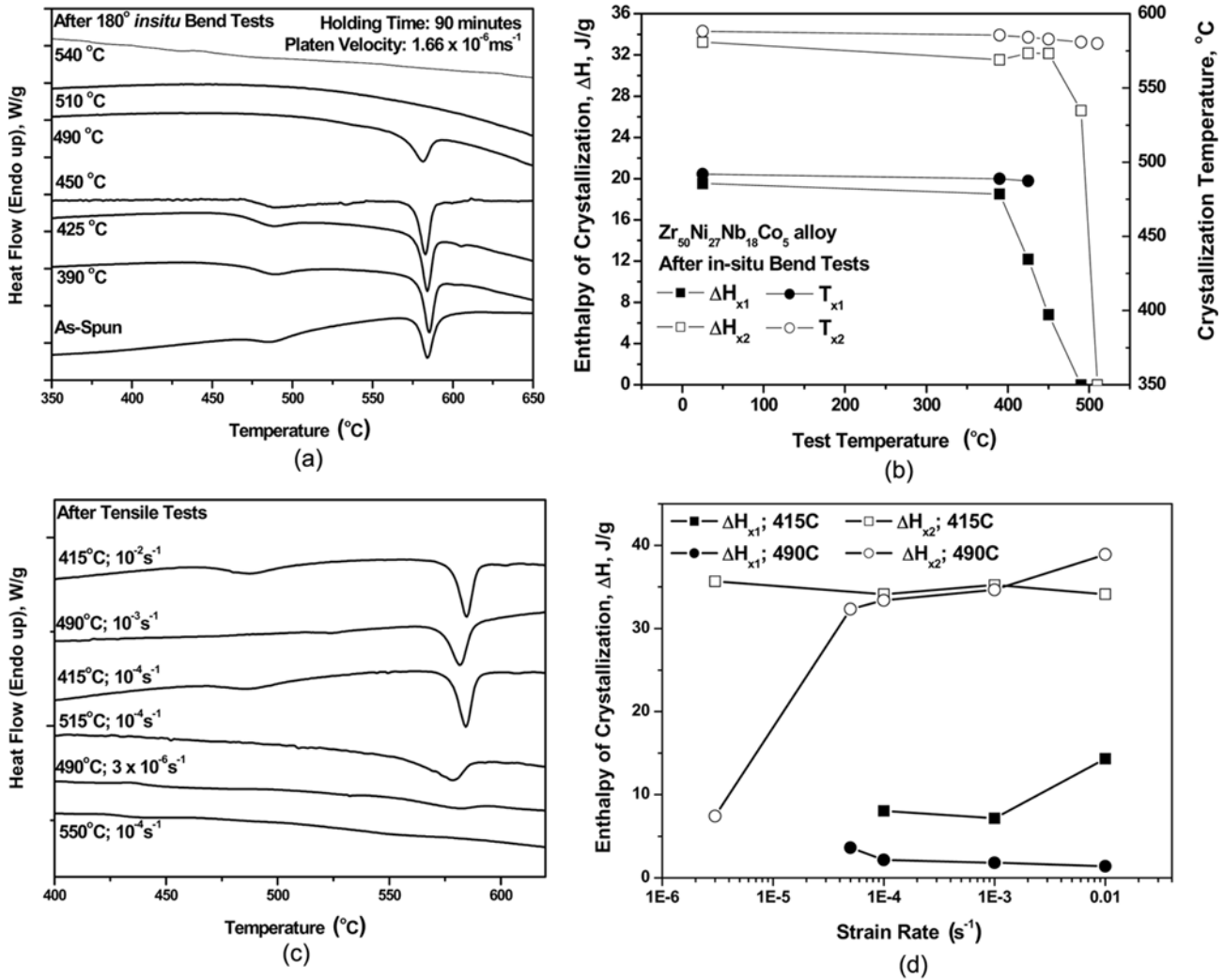
Fig. 6. DSC traces on the $Zr_{50}Ni_{27}Nb_{18}Co_5$ alloy after (a) bend tests and (c) tensile tests. (b) and (d) shows the influence of temperature and strain rate on the enthalpy of crystallization after mechanical tests.

applied test temperature during mechanical testing, the DSC traces in Fig. 6(c) (after tensile tests) show the influence of both the temperature and strain rate. From both cases, it can be seen that the application of external stress and temperature affects the thermal stability of the alloy. Throughout the temperature range tested, an increase in test temperature for a constant strain rate alters the thermal behavior significantly, as is evident from the results of the tests performed at 415 °C, 515 °C, and 550 °C under the strain rate of 10^{-4} s^{-1}. It is interesting to note that for 415 °C, which lies in the lower intermediate temperature regime (II) mentioned earlier (390 °C < T < 425 °C), the changes in DSC curves due to variation in the strain rate are not remarkable. However, for the Regime III (425 °C T 490 °C), which is the temperature range that results in large values of elongation, the influence of strain rate, i.e., time, is evident. For instance, the first crystallization peak vanishes when the strain rate decreases from 10^{-2}

s^{-1} to 10^{-6} s^{-1} at 490 °C, while that of the second peak is altered to a large extent. The effect of the imposed strain rate can also be seen by comparing the DSC traces of 490 °C at 10^{-6} s^{-1} with the one tested at a higher temperature and a higher strain rate (515 °C, 10^{-4} s^{-1}). If we further consider higher temperatures, for T >> 490 °C, the dominance of temperature over strain rate is clearly seen from the DSC traces of 515 °C, and that of 550 °C, for both tests were conducted at the same strain rate of 10^{-4} s^{-1}.

The variation of the enthalpies of crystallization for the Zr-Ni-Nb-Co ribbons with a strain rate is shown in Fig. 6(d). At 415 °C (Region II: 390 °C < T < 425 °C), the first crystallization temperature is slightly altered for tests that were performed at a low strain rate. In contrast, not only does the first peak vanishes at lower strain rates at 490 °C (Region III: 425 °C < T < 490 °C), but also a significant reduction in ΔH_{x2} is observed at lower strain rates. The observed changes in ther-

mal properties with strain rates are in accordance with the mechanical data observed in these temperature regimes.

Further, it can be observed from the T-T-T diagram (Fig. 1(c)) that the time-temperature dependence of the alloy can be divided into three regions. However, the temperature regimes obtained from the tensile tests, viz., T < 390 °C, 390 °C T 490 °C and T > 490 °C, are much lower than the ones obtained in the T-T-T diagram. According to Maddin and Masumoto [36], the application of tensile stress at an elevated temperature can facilitate the crystallization process. Kim [25] reported that the crystallization of a Cu-based bulk metallic glass during tensile loading at high temperature was strongly influenced by the environment and the strain, and the crystallization accelerated during deformation. In the present case, it should be noted that all mechanical tests were conducted in air, which would invariably influence the crystallization process. For example, it has been reported that in Zr-base binary alloys [37], the thermal analysis conducted in air shifted the onset of crystallization to the left (towards lower temperatures at significantly lower time) when compared to those performed under an argon atmosphere. This further proves that the crystallization process accelerated in an air atmosphere under the influence of stress. Hence, in the T-T-T diagram, determined from thermal analyses (Fig. 1(c)), the entire phenomenon would shift to lower times (and temperatures) during mechanical tests, implying that the formation of crystalline phases can take place at lower temperatures. This explains the discrepancy in temperatures seen in the T-T-T diagram and in those regimes obtained from the tensile tests.

Structural studies on the mechanically tested samples were also conducted by using X-ray diffraction and TEM observations. Figures 7(a) and (b) show the XRD patterns of the alloys after high temperature bend tests and tensile tests, respectively. While at room temperature the alloy shows a perfectly amorphous structure, increasing the temperature during bending tests introduces crystallization in the alloy (Fig. 7(a)). At lower temperatures, Zr_2Ni is the dominant phase (with lattice parameter a = b = 6.486 Å, c = 5.279 Å; space group: I4 /mcm), while ZrNi (with lattice parameter a = 3.257 Å, b = 9.944 Å, c = 4.118 Å; space group: Cmcm) and $Ni_{11}(Zr,Nb)_9$ compound forms at higher temperatures. Figure 7(b) shows the XRD profile after tensile tests. As both the mechanical tests were conducted in air, the oxidation of the alloy did occur (ZrO_2 formation) at all test temperatures. Table 1 shows the thickness of the oxide layer formed at 440 °C, in samples both without and with stress. Oxide thicknesses can reach upto few micrometers and it was observed that the applied stress accelerated the oxidation process. The analyses also indicated a dominant Zr oxide with Ni and Nb oxides as well. One can see that in Fig. 7(b), at 415 °C, ZrO_2 forms on the ribbon surface and is dominant along with a very low volume fraction of a Zr_2Ni nanocrystalline phase in the amorphous structure. However, at 490 °C the broad peak of the amorphous phase disappears to transform into a $Ni_{11}(Zr,Nb)_9$ crystalline phase (a = b = 9.880Å, c = 6.610Å; space group I4 /m). Much higher tem-

Table 1. Variation of oxide layer thickness in $Zr_{50}Ni_{27}Nb_{18}Co_5$ alloy, tested at 440 °C, with and without external applied stress

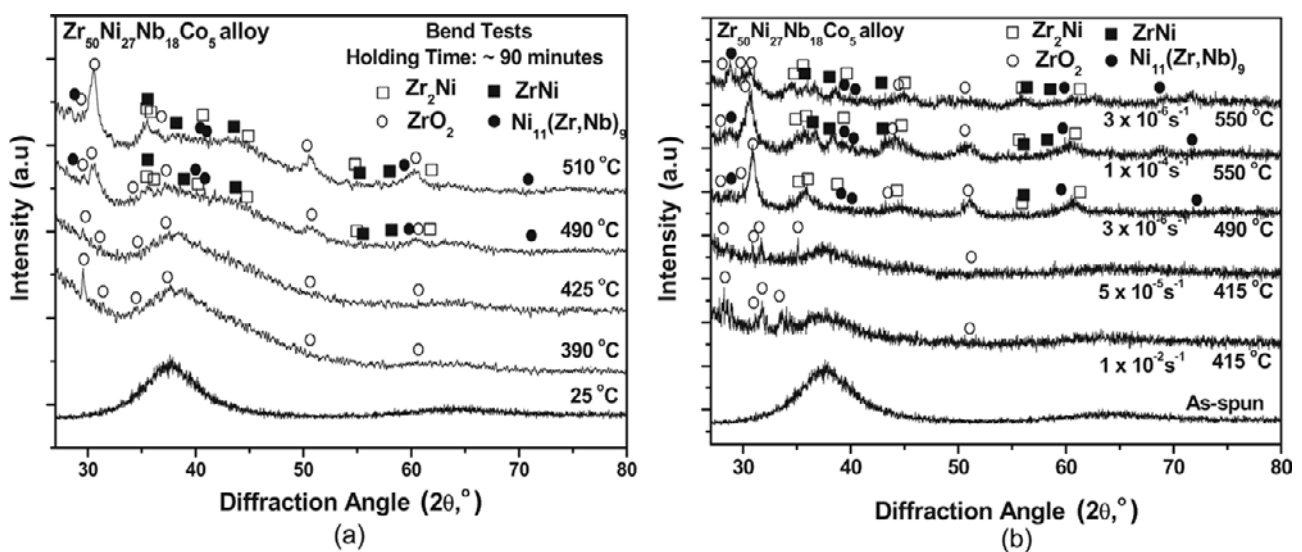| With stress (at 440 °C)	Oxide layer thickness	Without stress (at 440 °C)	Oxide layer thickness
$10^{-2}s^{-1}$ (26 min)	074 μm	26 min	910 nm
$10^{-4}s^{-1}$ (73 min)	1.56 μm	73 min	1.7 μm
$10^{-6}s^{-1}$ (215 min)	3.85 μm	215 min	2.9 μm

Fig. 7. XRD patterns of $Zr_{50}Ni_{27}Nb_{18}Co_5$ alloy (a) after bend tests at various temperatures and (b) after tensile tests with varying strain rates and temperatures.

peratures (T > 490 °C) can lead to the formation of several crystalline phases, (similar to Fig. 7(a)), which probably explains the brittle failure. Furthermore, Fig. 7(b) indicates that upon lowering the strain rate at a given temperature, the number of peaks of the same phase increases. This suggests that lower strain rates (i.e., longer time) aid in the growth of the pre-existing nuclei by allowing the diffusion of the nearest-neighbor atoms and favoring the local atomic rearrangement. Consequently, the presence of nano-crystals in the amorphous matrix led to higher values of the flow stress for tests that were performed under low strain rates, thus resulting in non-Newtonian flow. This microstructural change can also explain the plastic deformation observed at 290 °C under a strain rate of $3 \times 10^{-6} s^{-1}$, according to the nano-crystallization-induced deformation concept [38].

At this juncture, it is important to briefly state the deformation theories proposed for metallic glasses: 1) the free volume model proposed by Cohen and Turnbull [39], later developed by Spaepen [27], and 2) the Shear Transformation Zone (STZ) theory, initially proposed by Argon and Kuo [40], and further developed by Falk and Langer [41,42], are widely accepted. In the latter, the flow in amorphous metals is accommodated by cooperative shearing of atomic clusters, called as Shear Transformation Zones (STZ). However, the free volume plays an important role in that model too. STZ are likely to initiate in less packed clusters and the excess free volume tends to lower the deformation resistance of the sheared regions [43]. Although the concept of this model has been essentially used to explain and to model the room temperature behavior [41-44], it has recently been applied to take into account the Newtonian and non-Newtonian behavior of glass-former liquids in the supercooled liquid region [45,46].

The viscoplastic deformation is dependent on the atomic mobility that involves the rearrangement of a small number of atoms and their surrounding free volume [39]. In amorphous ribbons, the content of free volume is somewhat high due to its rapidly quenched structure. The larger the free volume, the easier is the atomic mobility that would favor a homogeneous flow [43]. It should also be noted here that, at high temperatures, the short-range diffusion of atoms would cause structural relaxation, and therefore a simultaneous reduction in free volume could not be neglected. However, Patterson and Jones [47] reported a reduction in the activation energy for crystallization upon application of a tensile stress. Hence, the cooperative shear model is believed to favor crystallization owing to the large atomic diffusion in an amorphous structure with relatively low stability, which prevents the achievement of the Newtonian flow, as well as the large elongation needed to fracture the Zr-Ni-Nb-Co amorphous ribbon.

Figure 8(a), (b), and (c) shows the TEM images of the alloys after mechanical tests at varying temperatures, falling in the three regions that were mentioned earlier. At room temperature, the alloy ribbon shows a perfectly amorphous structure (Fig. 8(a)-HRTEM image) with the selected area diffraction pattern (SADP, inset of Fig. 8(a)) showing a typical amorphous halo. In the intermediate temperature regime (Region III: 425° ≤ T ≤ 490 °C), where considerable plastic deformation has been observed, the presence of nanocrystals is evident (Fig. 8(b)). The Fast Fourier Transform image (FFT image – inset of Fig. 8(b)) shows several bright spots that are superimposed on the amorphous halo. The HRTEM image of the alloy at this temperature shows nanocrystals in the order of ~5 nm. Hence, in this temperature regime, the ribbon has a composite structure that is composed of nanocrystals that were dispersed in the amorphous matrix.

The nanocrystals would affect the mechanical behavior, for it is particularly expected that the nanocrystals would increase the flow stress of the ribbons. For a given tempera-
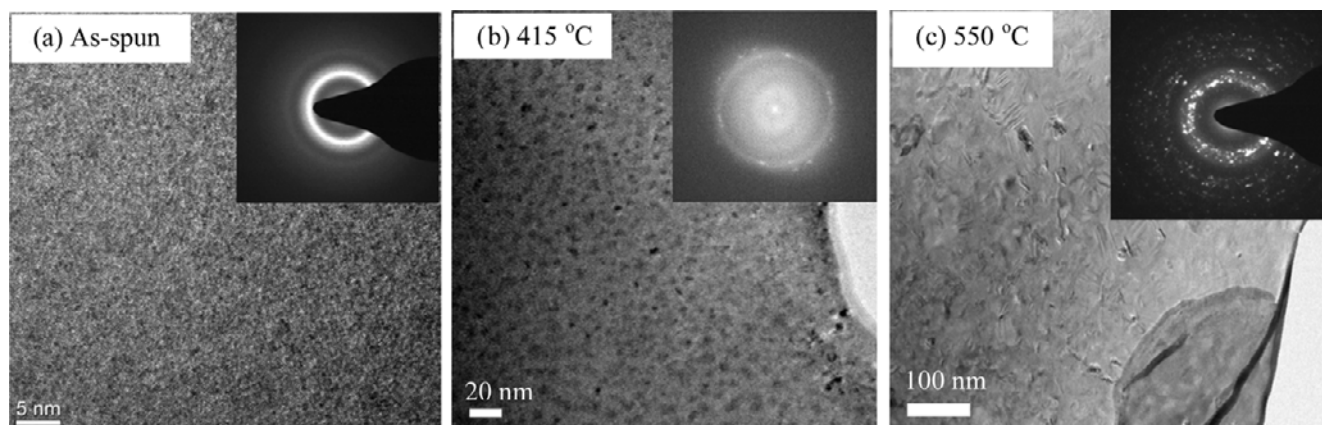

Fig. 8. (a) HRTEM image and SADP (inset) showing a fully amorphous structure of Zr₅₀Ni₂₇Nb₁₈Co₅ alloy in the as-received condition (b) TEM image of Zr₅₀Ni₂₇Nb₁₈Co₅ alloy tested at 415 °C showing nanocrystals of ~5nm dispersed in the amorphous matrix. Note the presence of several bright crystalline spots superimposed on the amorphous halo in the SADP (inset) (c) TEM image and SADP showing predominant crystallinity in the Zr₅₀Ni₂₇Nb₁₈Co₅ alloy tested at 550 °C.

ture in Region III (425° ≤ T ≤ 490 °C), the lower the strain rate, the larger the volume fraction of the nanocrystals is and the higher the flow stress. Hence, the nanocrystallization occurring during high temperature tensile tests is believed to be responsible for the non-Newtonian flow of this alloy. Indeed, the two different trends seen in Fig. 4(b), where 'm' decreases to exhibit a non-Newtonian behavior due to structural instability for T > 425 °C correlate well with the TEM observations, i.e., the nanocrystallization occurs at too low a temperature and thus hinders the Newtonian flow.

With further increase in temperature in addition to the nucleation of new crystals, the existing nanocrystals would grow in size, thereby increasing its volume fraction (which would further depend on the applied strain rate). The crystals that formed are in the order of 20 nm to 50 nm in size, with the SADP showing prominent crystalline spots, as observed in Fig. 8(c) for 550 °C. Also, note from Fig. 1(b) that the second crystallization peak has a lower activation energy, which would imply an easy crystallization. These nanocrystals, after reaching a critical value (of size and volume fraction), would give rise to internal residual stresses, which on application of an external tensile stress would lead to lowering the ductility [48] (brittleness induced by crystallization), as evident in Fig. 5 for T >> 490 °C. These structural transformations occurring at different temperature ranges support the observed differences in the mechanical behavior of the amorphous alloy at varying temperatures and strain rates.

The present study demonstrated that the $Zr_{50}Ni_{27}Nb_{18}Co_5$ amorphous ribbon maintains high strength and good ductility until 400 °C. In its potential application as a hydrogen permeable membrane, extending the operating temperatures up to 440 °C without any loss of mechanical integrity is also brought out. However, in order to be efficient for this application, the integrity of the alloy at these high temperatures will further be investigated in the presence of hydrogen.

5. CONCLUSIONS

The high temperature behavior of $Zr_{50}Ni_{27}Nb_{18}Co_5$ alloy has been studied in a wide range of temperature and strain rates. The highlights of the study can be summarized as follows:

The tensile behavior of the alloy could be divided into various temperature regimes following the severe dependency of strength on the test temperature.

Under tensile loading, at extreme low (T << 390 °C) and high temperatures (T >> 490 °C) from room temperature, the flow stress was insensitive to the strain rate.

At temperatures between 425 °C and 490 °C, the alloy exhibited a strain rate sensitivity, which does not follow Newtonian flow behavior.

The non-Newtonian behavior was attributed to the structural instability, which arose due to nanocrystallization dur-

ing deformation at high temperatures, as it hindered the viscous flow behavior. As evidenced from the deformation behavior, the mobility of atoms during cooperative shear was greatly influenced by the free volume, the application of tensile stress, and the experimental atmosphere (air).

From both the bend tests and tensile tests, in addition to oxidation, critical structural transformation occurred beyond ~ 440 °C that induced brittleness in the alloy.

The high strength and ductility of the Zr-Ni-Nb-Co ribbon up to 440 °C enable the application of this alloy for hydrogen permeation.

ACKNOWLEDGMENT

REFERENCES

1. J. Lu, G. Ravichandran, and K. L. Johnson, *Acta. mater.* **51**, 3429 (2003).
2. J. P. Chu, C. L. Chiang, T. Mahalingam, and T. G. Nieh, *Scripta mater.* **49**, 435 (2003).
3. X. L. Fu, Y. Li, and C. A. Schuh, *Acta mater.* **55**, 3059 (2007).
4. K. J. Laws, B. Gun, and M. Ferry, *Mater. Sci. Eng. A* **480**, 198 (2008).
5. K. C. Chan, L. Liu, and J. F. Wang, *J. Non Crystall. Solids* **353**, 3758 (2007).
6. Y. Saotome, Y. Noguchi, T. Zhang, and A. Inoue, *Mater. Sci. Eng. A* **375-377**, 389 (2004).
7. G. P. Zhang, Y. Liu, and B. Zhang, Scripta mater. **54**, 897 (2006).
8. D. S. Sung, *Master's Thesis*, Yonsei University, Seoul, Korea (2005).
9. S. Yamaura, Y. Shimpo, H. Okouchi, M. Nishida, O. Katija, H. Kimura, and A. Inoue, *Mater. Trans.* **44**, 1885 (2003).
10. S. Yamaura, Y. Shimpo, H. Okouchi, M. Nishida, O. Katija, and A. Inoue, *Mater. Trans.* **45**, 330 (2004).
11. Y. Shimpo, S. Yamaura, M. Nishida, H. Kimura, and A. Inoue, *J. Membrane Sci.* **286**, 170 (2006).
12. S. Yamaura, M. Sakurai, M. Hasegawa, K. Wakoh, Y. Shimpo, M. Nishida, H. Kimura, E. Matsubara, and A. Inoue, *Acta mater.* **53**, 3703 (2005).
13. X. Q. Guo, D. V. Louzguine, S. Yamaura, L. Q. Ma, W. Sun, M. Hasegawa, and A. Inoue, *Mater. Sci. Eng. A* **338**, 97 (2002).
14. S. Hara, K. Sakaki, N. Itoh, H. M. Kimura, K. Asami, and

A. Inoue, *J. Membrane Sci.* **164**, 289 (2000).

15. S. Jayalakshmi, K. B. Kim, and E. Fleury, *J. Alloy. Compds.* **417**, 195 (2006).

16. Yamaura, *Private Communication*.

17. D. Y. Lee, Y. C. Kim, E. Fleury, and Y. B. Kim, *Unpublished Results*.

18. S. Jayalakshmi, S. O. Park, K. B. Kim, E. Fleury, and D. H. Kim, *Mater. Sci. Eng. A* **449-451**, 920 (2007).

19. F. E. Luborsky and J. L. Walter, *J. Appl. Phys.* **47**, 3648 (1976).

20. S. Ashok, N. S. Stoloff, M. E. Glicksman, and T. Slavin, *Scripta metall.* **15**, 331 (1981).

21. M. A. Munoz-Morris, S. Surinach, L. K. Varga, M. D. Baro, and D. G. Morris, *Scripta mater.* **47**, 31 (2002).

22. Y. Kawamura, T. Shibata, A. Inoue, and T. Masumoto, *Mater. Trans. JIM* **40**, 335 (1999).

23. M. Heggen, F. Spaepen, and M. Feuerbacher, *J. Appl. Phys.* **97**, 033506 (2005).

24. Y. Kawamura, T. Shibata, A. Inoue, and T. Masumoto, *Appl. Phy. Lett.* **69**, 1208 (1996).

25. W. J. Kim, *Intermetallics* **15**, 282 (2007).

26. A. V.Sergueeva, N. A. Mara, J. D. Kuntz, E. J. Lavernia, and A.K. Mukherjee, *Phil. Mag.* **85**, 2671 (2005).

27. T. G. Nieh, C. Schuh, J. Wadsworth, and Y. Li, *Intermetallics* **10**, 1177 (2002).

28. F. Spaepen, *Acta metall.* **25**, 407 (1977).

29. C. L. Chiang, J. P. Chu, C. T. Lo, T. G. Nieh, Z. X. Wang, and W. H. Wang, *Intermetallics* **12**, 1057 (2004).

30. D. H. Bae, H. K. Lim, S. H. Kim, D. H. Kim, and W. T. Kim, Acta mater. **50**, 1749 (2002).

31. V. Ocelik, Y. V. Fursova, V. A. Khonik, and K. Csach, *Phys.*

Solid State **42**, 697 (2000).

32. W. J. Kim, Y. K. Sa, J. B. Lee, and H. G. Jeong, *Intermetallics* **14**, 1391 (2006).

33. Y. Kawamura, T. Shibata, A. Inoue, and T. Masumoto, *Scripta mater.* **37**, 431 (1997).

34. P. Chu, C. L. Chiang, T. G. Nieh, and Y. Kawamura, *Intermetallics* **10**, 1191 (2002).

35. T. Mukai, T. G. Nieh, Y. Kawamura, A. Inoue, and K. Higashi, *Scripta mater.* **46**, 43 (2002).

36. R. Maddin and T. Masumoto, *Mater. Sci. Eng.* **9**, 153 (1972).

37. H. M. Kimura, K. Asami, A. Inoue, and T. Masumoto, *Corr. Sci.* **35**, 909 (1993).

38. S. W. Lee, M. Y. Huh, E. Fleury, and J. C. Lee, *Acta mater.* **54**, 349 (2006).

39. M. H. Cohen and D. Turnbull, *J. Chem. Phys.* **31**, 1164 (1975).

40. A. S. Argon and H. Y. Kuo, *Mater. Sci. Eng.* **39**, 101 (1979).

41. M. L. Falk and J. S. Langer, *Phys. Rev. E.* **57**, 7192 (1998).

42. J. S. Langer, *Scripta mater.* **54**, 275 (2006).

43. A. S. Argon, *Acta metall.* **27**, 17 (1979).

44. Y. Shi, M. B. Katz, H. Li, and M. L. Falk, *Phys. Rev. Lett.* **98**, 185505 (2007).

45. J. S. Langer and A. Lemaıtre, *Phys. Rev. Lett.* **94**, 175701 (2005).

46. M. Demetriou, J. S. Harmon, M. Tao, G. Duan, K. Samwer, and W. L. Johnson, *Phys. Rev. Lett.* **97**, 065502 (2006).

47. J. Patterson and D. R. H. Jones, *Scripta metall.* **13**, 947 (1979).

48. A. Sergueeva, N. Mara, and A. K. Mukherjee, *J. Non-Crystall. Solids* **317**, 169 (2003).